PAPER

Check for updates

Improving light absorption and photoelectrochemical performance of thin-film photoelectrode with a reflective substrate†

Jingran Xiao, [ID] *[a] Lingling Peng,[a] Le Gao, [ID] [a] Jun Zhong,[a] Zhongliang Huang,[a] Enxian Yuan,[b] Vijayan Srinivasapriyan,[c] Shu-Feng Zhou[a] and Guowu Zhan [ID] *[a]

The charge separation/transport efficiency is relatively high in thin-film hematite photoanodes in which the distance for charge transport is short, but simultaneously the high loss of light absorption due to transmission is confronted. To increase light absorption in thin-film Fe_2O_3:Ti, commercial substrates such as Cu foil, Ag foil, and a mirror are adopted acting as back-reflectors and individually integrated with the Fe_2O_3:Ti electrode. The promotion effect of the commercial back-reflectors on the light absorption efficiency and photoelectrochemical (PEC) performance of the hydrothermally prepared Fe_2O_3:Ti electrodes with a variety of film thicknesses is investigated. As a result, Ag foil and the mirror show favorable and equal efficacy while the promoting effect of Cu foil is limited. In addition, the photocurrent increment achieved by the Ag back-reflector decreases linearly along with the logarithmic of the film thickness and the optimized film thickness of the Fe_2O_3:Ti electrode is decreased from 520 to 290 nm. The high durability of Ag foil in the alkaline electrolyte during solar light irradiation is demonstrated. Furthermore, the reflective substrate also shows a promotion effect on the $BiVO_4$ photoanode and $CuBi_2O_4$ photocathode, as well as the unbiased photocurrent from a tandem cell constituted by TiO_2 and $CuBi_2O_4$.

1. Introduction

The photoelectrochemical (PEC) water splitting process is one of the most promising options for solar light conversion direct into available chemicals and has attracted extensive attention in the research field.[1–3] Researchers focus particularly on the water oxidation reaction since it involves four electrons and is of higher difficulty than the water reduction counterpart. Various photoanode materials have been intensively studied, including TiO_2, $BiVO_4$, α-Fe_2O_3, WO_3, *etc*, among which α-Fe_2O_3 possesses superiority in that it is low cost, non-toxic and has high stability in neutral and basic electrolytes, and most importantly is one of the most applicable photoanode materials with a theoretical photocurrent density up to 12.6 mA cm^{-2}.[4–9] However, the known practical photocurrent density of the α-Fe_2O_3 photoanode is still less than 3 mA cm^{-2} at 1.23 V_{RHE} (*versus* reversible

[a]College of Chemical Engineering, Huaqiao University, 668 Jimei Blvd, Xiamen, Fujian, 361021, P. R. China. E-mail: xjr@hqu.edu.cn; gwzhan@hqu.edu.cn

[b]School of Chemistry and Chemical Engineering, Yangzhou University, Yangzhou, Jiangsu 225002, P. R. China

[c]Key Laboratory of Nanosystem and Hierarchical Fabrication, CAS Center for Excellence in Nanoscience, National Center for Nanoscience and Technology, Beijing 100190, China

hydrogen electrode).[10,11] This should be partly due to the low charge transfer efficiency and high onset potential caused by sluggish water oxidation kinetics with the strong Fermi level pinning effect of surface states.[12,13] Besides, the carrier mobility in α-Fe_2O_3 is merely 0.01 cm^2 V^{-1} s^{-1} due to its poor intrinsic conductivity. Therefore, severe bulk charge recombination occurs in hematite photoanode which thereby limits the charge separation and transport efficiency.[14,15]

To address this issue, an intensive effort has been denoted to reduce the onset potential of α-Fe_2O_3 photoanode by passivation of surface states with a functional oxide layer (*e.g.* TiO_2,[16] Ga_2O_3,[17] Al_2O_3,[18] *etc.*) or acceleration of the oxidation reaction kinetics by the assistance of an oxygen evolution reaction (OER) catalyst.[19–22] For instance, an impressively low onset potential of 0.45 V_{RHE} has been reported by Wang's group realized by a re-growth α-Fe_2O_3 photoanode loaded by $NiFeO_x$ catalyst.[23] In the meantime, the low-bias performance of α-Fe_2O_3 photoanodes is seen to have significant progress,[24] and that the high-bias surface charge transfer efficiency can reach 100%.[25,26] It appears that to conquer the bulk charge[27] recombination is more challenging since the bulk charge separation/transport efficiency is still lower than 30%,[28,29] though conventional efforts including element doping,[30–32] nanostructure control,[33,34] and heterojunction fabrication[35–37] have been devoted.

Computational and experimental work has been focused on the super-thin α-Fe_2O_3 photoanode. The hole collection depth

in α-Fe_2O_3 is only ~12 nm, with hole diffusion length of ~5 nm and space charge layer width of ~7 nm.[38] In the super-thin α-Fe_2O_3 photoanode, film thickness matches the hole collection length, thereby reducing the probability of charge recombination and improving the charge transport efficiency.[39] However, most photons are wasted due to strong light transmission through super-thin α-Fe_2O_3, thus limiting the light absorption efficiency. To address this problem, researchers have been attempting to enhance light absorption efficiency by optical means. The concept is to either construct a light diffuse layer to trap the photons on the electrode by changing the direction of photons or adopt a specular reflection layer to simply accomplish secondary light absorption by light reflection. Li et al.[40] and Kim et al.[41] prepared α-Fe_2O_3 thin-film photoanodes on a three-dimensional (3D) FTO substrate, which achieved significant improvement in light absorption and PEC performance. As a fact, the applications of optical patterning substrate for tunable optical reflectance has been successfully applied in photovoltaic, PEC, and light-emitting diode fields.[42,43] Dotan et al.[44] provided a strategy by deposition of a back-reflection layer between the FTO layer and glass substrate, which also efficiently heightened the light availability in super-thin α-Fe_2O_3 photoanode. However, it must be admitted that the manufacturing of 3D FTO or deposition of a reflective sub-layer is highly equipment dependent, technically difficult and too costly for real industrial applications.

Herein, to avoid using the costly equipment, we report a facile and versatile strategy by adopting commercial light-reflective substrates such as Cu foil, Ag foil and mirror which were individually assembled with the FTO glass acting as back-reflectors. The thickness of the Fe_2O_3:Ti nanorod electrode prepared hydrothermally was controlled from 180 to 650 nm via a hydrothermal method and the light absorption efficiency and PEC performance affected by film thickness were fully discussed. Also, the promoting effect of the back-reflectors was determined, which decreased as increasing the film thickness. The high stability of the reflective substrate provides a long-term guarantee for performance improvement. Besides, the reflective substrate shows high flexibility and universality in various photoelectrodes and tandem system. We put a concept here that a simple integration of photoanode with a reflective substrate can significantly improve the PEC performance.

2. Experimental section

2.1 Chemicals

The chemicals and reflective substances were purchased and used without any further purification, including the iron(III) chloride hexahydrate ($FeCl_3 \cdot 6H_2O$, 99.0%, Aladdin), titanium(IV) butoxide ($C_{16}H_{36}O_4Ti$, 99%, Adamas), methanol (CH_3OH, 99.9%, Adamas), anhydrous sodium acetate (CH_3COONa, 98.0%, Guangfu), sodium ferrocyanide ($Na_4Fe(CN)_6$, AR, Macklin), cupric nitrate trihydrate ($Cu(NO_3)_2 \cdot H_2O$, AR, Xilong), bismuth nitrate pentahydrate ($Bi(NO_3)_3 \cdot 5H_2O$, 98%, Sigma-Aldrich), nitric acid (HNO_3, 70%, Sinopharm), ammonium vanadate (NH_4VO_3, 99%, Adamas), hydrochloric acid (HCl, 37%, Sinopharm), ethanol (CH_3CH_2OH, AR, Xilong), acetic acid (CH_3COOH, 99%, Adamas).

2.2 Synthesis of the Fe_2O_3:Ti electrodes

The synthesis and modification methods of the Fe_2O_3:Ti electrodes on FTO substrates were similar to our previous report.[45] Briefly, clean FTO glasses were immersed in a solution of 0.09 M $FeCl_3 \cdot 6H_2O$ and 0.1 M CH_3COONa (230 uL HCl added to adjust pH to 1.45) and hydrothermally treated at 95 °C before immersing in 0.5% v/v titanium(IV) butoxide ethanol solution for ~2 s and calcined at 550 °C for 2 h and further annealed at 750 °C for 15 min. Then, the obtained Fe_2O_3:Ti electrodes were solvothermal treated in absolute methanol at 180 °C for 12 h. For thickness adjustment, the hydrothermal time was controlled to 120, 130, 135, 150, and 180 min. The reflective substrate was integrated with each Fe_2O_3:Ti electrodes independently by overlaying at the back-side of FTO.

The Au deposition on the Fe_2O_3:Ti electrode was done on a sputter coater (Cressington 108Auto).

2.3 Synthesis of other electrodes

TiO_2 electrode was prepared hydrothermally according to the previous report.[46] In brief, FTO was immersed in a mixture of 0.4 mL titanium(IV) butoxide, 15 mL DI water and 15 mL concentrated HCl under stirring. After the hydrothermal reaction at 160 °C for 4 h and calcination at 600 °C for 2 h, the TiO_2 electrode was obtained. $BiVO_4$ electrode was prepared by a seed layer assisted hydrothermal reaction at 180 °C for 12 h with $Bi(NO_3)_3 \cdot 5H_2O$ and NH_4VO_3 as the Bi and V sources, followed by calcination at 450 °C for 2 h.[47] The $CuBi_2O_4$ electrode was made by drop-casting the solution of $Cu(NO_3)_2 \cdot H_2O$ and $Bi(NO_3)_3 \cdot 5H_2O$ dissolving in ethanol/acetic acid mixture on FTO with an amount of 20 μL cm^{-2} and then calcining at 550 °C for 2 h.

2.4 Photoelectrochemical measurements

The PEC measurements of the electrodes for Fe_2O_3:Ti, TiO_2 and $CuBi_2O_4$ electrodes were performed at room temperature on the electrochemical workstation (CHI 660D, CH Instruments) with a three-electrode connection of platinum mesh as the counter electrode, Hg/HgO (1 M KOH) as the reference electrode, 1 M NaOH solution (pH 13.6) as the electrolyte with the electrodes facing to simulated sunlight (AM 1.5G, 100 mW cm^{-2}). The $BiVO_4$ electrode was tested similarly but in PBS solution (pH 7.4) with Ag/AgCl (3 M KCl) as the reference electrode. Tandem PEC cell contains a two-electrode configuration of TiO_2 as the working electrode and $CuBi_2O_4$ as the counter electrode. The bias-free photocurrent was measured at 0 V with light irradiating on the TiO_2 photoanode and then the rear $CuBi_2O_4$ photocathode. The light was irradiated from a xenon lamp (PerfectLight, PLS-SXE300D) which was equipped with an AM 1.5G light filter and a light shutter.

The polarization curves were scanned at 20 mV s^{-1}. Chronoamperometry was tested at 1.23 V_{RHE} to verify the stability of the Fe_2O_3:Ti photoanodes with and without the reflective substance.

Cyclic voltammetry (CV) test was performed at scan rates from 20 to 120 mV s^{-1} and the electrochemical surface area (ECSA) was calculated with half the linear slope of the capacitive current versus scan rate.[48]

RSC Advances

Incident-photon-to-current conversion efficiency (IPCE) was measured at 1.23 V_{RHE} using bandpass filtered light from 350 to 700 nm and calculated by eqn (1):[49]

$$IPCE = (1240J)/(\lambda J_{light}) \tag{1}$$

where J is the photocurrent density, λ is the incident light wavelength, and J_{light} is the measured power density of incident light.

Theoretical photocurrent density (J_{abs}) was estimated by eqn (2):[50]

$$J_{abs} = \int_{\lambda_1}^{\lambda_2} LHE \frac{\lambda}{1240} P_{abs(\lambda)} d_\lambda \tag{2}$$

where $P_{abs(\lambda)}$ is the solar irradiance at AM 1.5G as a function of wavelength λ and LHE is the light-harvesting efficiency.

Charge transfer efficiency (η_{tran}) was defined as the generated photocurrent density to J_{abs} ($\eta_{tran} = J/J_{abs}$).

All the potentials were relative to the reversible hydrogen electrode (RHE) by using the Nernst equation:

$$E_{RHE} = E_{Hg/HgO} + E_{ref}^{\theta} + 0.0592 \text{ pH} \tag{3}$$

$E_{Hg/HgO}^{\theta}$ and $E_{Ag/AgCl}^{\theta}$ were respectively determined to be 0.014 V and 0.2 V through the cyclic voltammetry scanning of 1 mM aqueous solution of $Na_4Fe(CN)_6$.

2.5 Characterizations

The X-ray diffraction (XRD) patterns of the samples were measured at a scan rate of 8° min^{-1} on a Rigaku SmartLab X-ray diffractometer with the Cu Kα radiation (40 kV × 30 mA). The surface and cross-section morphology of the electrodes were measured on a HITACHI SU5000 thermal field emission scanning electron microscope (SEM). The light-harvesting efficiency of the electrodes and light reflection efficiency of the reflective substrates were investigated on an Agilent Cary500 spectrometer in diffuse reflection pattern.

3. Results and discussion

3.1 Fe$_2$O$_3$:Ti electrodes with different thicknesses

The Fe$_2$O$_3$:Ti electrodes fabricated hydrothermally with a variation of the hydrothermal time were photographed and showed a tendency of colour to get deeper from light yellowish-brown to dull red (inset in Fig. 1), indicating the increase of film thickness. The XRD pattern of the electrodes in Fig. 1 was well-indexed to tetragonal SnO$_2$ and hexagonal Fe$_2$O$_3$. The intensity of the strong peaks of SnO$_2$ stemmed from the FTO substrate was identical for all the samples. It is noted that Fe$_2$O$_3$ showed a highly dominant orientation of (110) crystal plane along with a weak peak of (330) plane and a negligible peak of (104) plane. The increase in the intensity of (110) and (330) planes was in coincidence with the prolonged hydrothermal time, which also suggests the constant orientation of Fe$_2$O$_3$ during growth.

SEM images of the Fe$_2$O$_3$:Ti electrodes in vertical and cross-section views are displayed in Fig. 2, all showing a nanorod morphology with a diameter of tens of nanometres. However, as
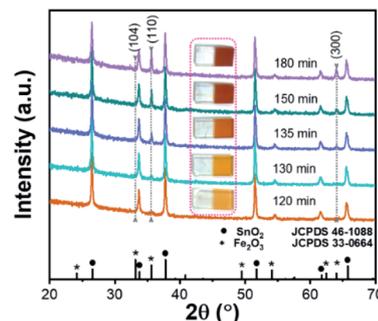

Fig. 1 XRD patterns and photographs (inset) of the Fe$_2$O$_3$:Ti electrodes prepared by adjusting the hydrothermal time.

hydrothermal time increases, the nanorods became more compact and the diameter of the nanorods increased (from ~50 to ~80 nm), which was especially evidenced from the comparison of Fig. 2b and c. Fig. 2d and e give evidence that adhesion among the nanorods occurred when the film is too thick. The thickness of the electrodes was measured to 180, 250, 330, 520, and 650 nm, respectively, according to the cross-section images (Fig. 2f–j). According to the correlation between Fe$_2$O$_3$:Ti film thickness and hydrothermal reaction time (Fig. S1†), film thickness increase was fast at the beginning and then became slower, which conforms to common growth kinetics.

The nanostructure morphology of the Fe$_2$O$_3$:Ti electrodes contributes to a relatively high electrochemical specific surface area (ECSA), as seen from the CV curves in Fig. S2a–e† and the calculated results in Fig. 3a and S2f.† The ECSA was increased as the film became thicker. However, the increase rate of ECSA was rapid for the thin films and slowed down gradually when the film gets thick, which is understandable because the incremental amount and length of the nanorods in the thin films dedicated to most of the surface areas while the adhesion
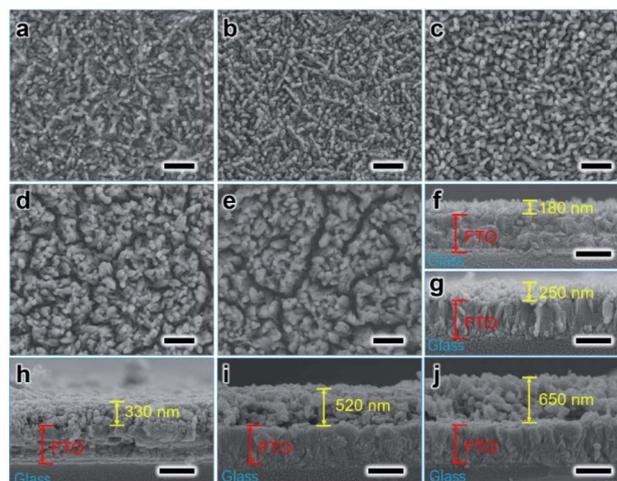

Fig. 2 Verticle (a–e) and cross-section (f–j) SEM view of the Fe$_2$O$_3$:Ti electrodes prepared by adjusting the hydrothermal time; (a and f) 120 min; (b and g) 130 min; (c and h) 135 min; (d and i) 150 min; (e and j) 180 min. Scale bars are 500 nm.
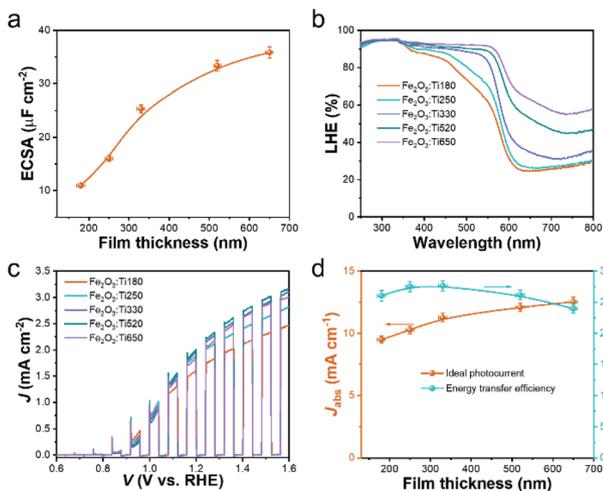
Fig. 3 (a) The estimated electrochemical specific surface area (ECSA), (b) the light-harvesting efficiency (LHE), and (c) the polarization curve of the Fe_2O_3:Ti electrodes with the thickness of 180, 250, 330, 520 and 650 nm (named as Fe_2O_3:Ti$_n$, n represents the film thickness); (d) variation of the calculated theoretical photocurrent (J_{abs}) and charge transfer efficiency (η_{tran}) as a function of the film thickness. All the Y-axis error bars in this work were counted by measurements of three parallel specimens and the X-axis error bars were the measuring error of 10 nm.

of nanorods in thick films was inconducive to the surface area, as indicated in Fig. 2. An enhancement in light-harvesting efficiency (LHE) of the Fe_2O_3:Ti electrodes was achieved with increasing film thickness, which was well expressed at a range of 350 to 610 nm (the absorption edge of Fe_2O_3:Ti), as illustrated in Fig. 3b. The inescapable tail of LHE at 610 to 800 nm is due to the absorption of bare FTO (Fig. S3a†). As an apparent view in Fig. 3b, the LHE of Fe_2O_3:Ti$_{650}$ exceeded absorbance of 90% below 610 nm, where the waste of the rest photons should be due to inevitable reflectance rather than transmission, as suggested by the stagnant absorptance in the UV range. That is, the transmittance of prepared Fe_2O_3:Ti electrodes varied from a high level to zero.

The PEC performance of the Fe_2O_3:Ti electrodes was measured in terms of the light chopped polarization curve scanned at 20 mV s^{-1} and plotted in Fig. 3c. All the samples showed a typical curve of the Ti-doped Fe_2O_3 photoanode with an onset potential of ~0.85 V and a negligible dark current. The Fe_2O_3:Ti$_{180}$ electrode showed a favorable photocurrent density of 2.3 mA cm^{-2} at 1.6 V_{RHE}. As increasing the thickness, the photocurrent was enhanced to a maximum of 3.0 mA cm^{-2} at 1.6 V_{RHE} by the Fe_2O_3:Ti$_{520}$ electrode and then decreased marginally. The highest photocurrent density achieved by the Fe_2O_3:Ti$_{520}$ electrode was a result of balancing the light absorption and charge transfer efficiency. Assuming 100% absorbed photon-to-current efficiency, the theoretical photocurrent densities (J_{abs}) were simulated by weighing the solar light irradiance with LHE (Fig. S3b†). Then the experimental photon-to-current efficiency, that is the charge transfer efficiency (η_{tran}), was calculated with the photocurrent density at 1.6 V_{RHE} divided by J_{abs}. The values of J_{abs} and η_{tran} following

film thicknesses are compared in Fig. 3d. The J_{abs} increased considerably when thickness increased from 180 to 330 nm while less increase was seen for the thicker films, indicating that a thin part of the Fe_2O_3:Ti film contributes to most of the light absorbance. As for the η_{tran}, it showed in a volcano shape with a maximum achieved by the Fe_2O_3:Ti$_{290}$ electrode. Since the η_{tran} is promoted in the nanorods where the hole diffusion distance is short, the increase in the thin films and the decrease in the thick films of η_{tran} along with film thickness are attributed to the formation of more nanorods and the adhesion of nanorods, respectively. Considering both the J_{abs} and η_{tran}, the excess increase of film thickness contributes little to light-harvesting and is at a cost of a loss of charge transfer efficiency.

3.2 The improvement effect of reflective substances

To lift the light absorption of the Fe_2O_3:Ti electrodes, we simply integrated a reflective substance along with the FTO glass to reflect the transmitted photon for reabsorption by Fe_2O_3:Ti. The polished Cu foil, Ag foil and the CM were used, and their photography and reflectance spectra are depicted in Fig. S4a.† It shows that each has a degree of reflex in UV-visible range, but Cu foil exhibited a weak reflection of photons with $\lambda < 550$ nm and the Ag foil and CM showed a favorable reflection of photons with wavelengths above 330 and 350 nm respectively. Moreover, CM had higher reflection than the Ag foil in wavelength between 360 and 530 nm. Fig. 4a exhibits the reflection result of the three reflective substances on the Fe_2O_3:Ti$_{180}$ electrode. It is observed that the Ag foil and CM showed a similar promoting effect on the light absorption of the Fe_2O_3:Ti electrode. The higher light absorption of Cu foil supported electrode was unreliable since Cu had strong self-ability of absorption, which
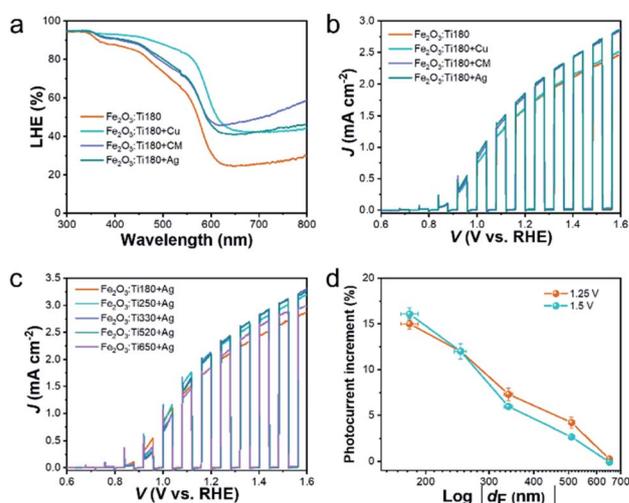

Fig. 4 (a) LHE and (b) polarization curve of the bare Fe_2O_3:Ti$_{180}$ electrode and those supported by Cu foil, Ag foil and commercial mirror (CM); (c) the polarization curves of the Fe_2O_3:Ti electrodes with Ag back-reflector; (d) the calculated photocurrent density increment at certain bias potentials as a function of the logarithm of film thickness (d_F) thanks to the light reflection of Ag foil.

can be confirmed by the PEC performance shown in Fig. 4b. The improvement of photocurrent was merely 2% assisted by Cu foil, while that was 15% for electrodes with Ag and CM back-reflectors. Regarding that Ag foil and CM showed an almost equal effect on both light-harvesting and the photocurrent density, their function is indicated to merely result from the light reflection effect. Then, the performance of the electrodes of different thickness with and without Ag back-reflector was compared (Fig. S5†). As a whole, all the electrodes realized a performance enhancement after assembling the Ag back-reflector except for the $Fe_2O_3:Ti_{650}$ which should have reached saturation of light absorption, and the photocurrent increment decreases as increasing the film thickness. For the performance comparison of the Ag foil supported electrodes depicted in Fig. 4c, although the performance has been remarkably enhanced of the $Fe_2O_3:Ti_{180}$ and $Fe_2O_3:Ti_{250}$ electrodes with thinner films, the championship of the $Fe_2O_3:Ti_{520}$ electrode was not shaken. However, it is undeniable that the $Fe_2O_3:Ti_{260}$ and $Fe_2O_3:Ti_{290}$ electrodes showed comparable and equal performance in comparison with $Fe_2O_3:Ti_{520}$. It suggests that the Ag back-reflector indeed expressed its availability, but still with limited effectiveness on performance enhancement of the $Fe_2O_3:Ti$ electrode. On a view of the photocurrent increment of the electrodes with Ag reflector at certain bias potentials, as indicated in Fig. 4d, the photocurrent increment at 1.25 and 1.5 V was similar and decreased from about 15% of the $Fe_2O_3:Ti_{180}$ electrode to zero of the $Fe_2O_3:Ti_{650}$. An approximate linear relation was found between the photocurrent increment and the logarithmic of the film thickness, which is coincident with the previous result that the photon flux in a layer of $Fe_2O_3:Ti$ follows a logarithmic relationship with the film thickness.[44] A control sample with a deposition of an Au reflective layer on the back-side of $Fe_2O_3:Ti_{180}$ was also prepared. As seen in Fig. S6,† there was a 4% photocurrent increase after Au layer deposition, much less than the Ag reflector, indicating that the light reflection efficiency of a reflective substrate can be much higher than the deposited reflective layer.

The incident photon-to-electron conversion efficiency (IPCE) of the $Fe_2O_3:Ti$ electrodes without the Ag back-reflector are plotted in Fig. 5a. With the film thickness increases from 180 to 250 nm, the enhancement of IPCE was approximately equivalent to 10% at each wavelength of the incident photon. Meanwhile, the enhancement at the UV range was negligible but became more significant at the visible light range when the film thickness further increased, which is observably told as comparing the $Fe_2O_3:Ti_{260}$ and $Fe_2O_3:Ti_{290}$ electrodes. This phenomenon is coincident with the UV-vis spectra, again confirming that light absorption at short wavelength is easier to reach a saturation state. It is also noted that the quantum efficiency of photoanode $Fe_2O_3:Ti_{650}$ was lower at the whole wavelength of photons than $Fe_2O_3:Ti_{520}$, which is due to the low charge conversion efficiency rather than the light absorption and thus independent of the photon wavelength. When the Ag back-reflector was adopted, the escalation of IPCE for each photoanode of different film thickness, as can be observed in Fig. S7,† followed the same trend with photocurrent density, which again expressed the boosted photon conversion. It also indicated that the back-reflector was effective in the whole tested light absorption range. As a result (Fig. 5b), the difference in IPCE among the various $Fe_2O_3:Ti$ electrodes using an Ag back-reflector dwindled, no matter at the UV or the visible light range. The approximately identical IPCE of the $Fe_2O_3:Ti_{260}$, $Fe_2O_3:Ti_{290}$ and $Fe_2O_3:Ti_{520}$ were found with a maximum of around 74.8%.

Based on the above results, Fig. 6 depicts a simplified sketch of Ag back-reflector affecting the PEC performance of the $Fe_2O_3:Ti$ photoanode. For a thin layer of bare $Fe_2O_3:Ti$ nanorod photoanode, the light conversion efficiency is high, but the light absorption efficiency is limited due to strong transmission. With the increase of the film thickness, the light absorption is enhanced but at a loss of charge transfer efficiency. A trade-off between light absorption and charge transfer efficiency appears to be inevitable. In the meantime, the absorption of UV light reaches saturation for the film with a thickness of 260 nm, so the further increase of film thickness enhances light absorption more significantly in the visible light region. However, encouragingly, when an Ag foil (or a commercial mirror) is integrated acting as a light back-reflector, the transmitted photons of $\lambda > 350$ nm can be reflected through the $Fe_2O_3:Ti$ layer to achieve re-absorption and then improve the PEC performance. As a fact, the promoting effect of the Ag reflector is very similar to the increase of film thickness except for the independence of photon wavelength.
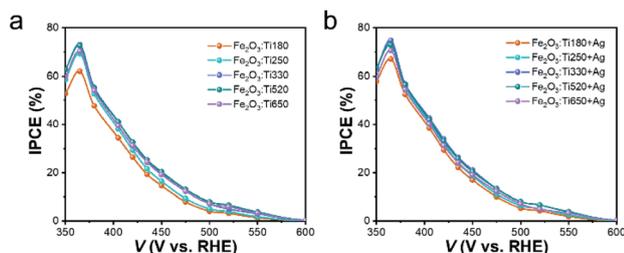

Fig. 5 Comparison of the incident photon-to-electron conversion efficiency (IPCE) of the $Fe_2O_3:Ti$ electrodes of different thicknesses (a) with and (b) without Ag back-reflector.
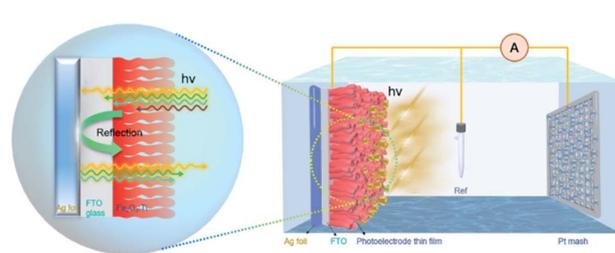

Fig. 6 Schematic diagram of the PEC water splitting system and the promoting effect of the Ag reflective substance on the light absorption of $Fe_2O_3:Ti$ electrode.

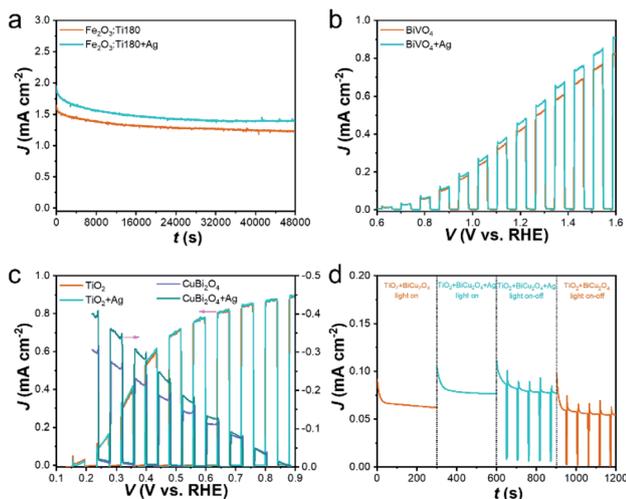Fig. 7 (a) Long-term stability of photoanode Fe_2O_3:Ti_{180} with and without the Ag reflective substrate; comparison of the polarization curves of the (b) $BiVO_4$ photoanode, (c) TiO_2 photoanode and $CuBi_2O_4$ photocathode with and without the Ag reflective substrate; (d) chronoamperometry test of the TiO_2//$CuBi_2O_4$ tandem cell under zero bias with and without the Ag reflective substrate integrated with $CuBi_2O_4$.

3.3 Stability and universal applications of the reflective substance

The promoting effect of the reflective substrate has been proved. To verify its durability during photoirradiation in the highly alkaline electrolyte, the prolonged photocurrent of the Fe_2O_3:Ti_{180} photoanode with and without the Ag reflector was measured (Fig. 7a). A photocurrent decay of Fe_2O_3:Ti_{180} was observed, which is similar to our previous result.[45] After the integration of Ag foil, a higher photocurrent was achieved, and the decreasing variation of photocurrent followed the same trend as the bare one. Therefore, the high stability of the Ag reflector during the PEC test is determined.

Since the promotion effect of the reflective substrate is attributed by light reflection, theoretically it can show availability on all the photoelectrodes with a thin-film or incomplete light absorption. The extensively studied $BiVO_4$, TiO_2 photoanode and $CuBi_2O_4$ photocathode were prepared and used as additional photoelectrode models. The SEM images (Fig. S8†) indicate that polyhedral $BiVO_4$, nanorod-like TiO_2 and porous $CuBi_2O_4$ were obtained, which showed a thickness of ∼360, ∼750, and ∼500 nm, respectively. According to

UV-vis spectra (Fig. S9†), the absorption edge of $BiVO_4$, TiO_2 and $CuBi_2O_4$ are around 520, 415 and 675 nm, respectively. With the integration of an Ag reflector, the electrodes showed enhanced light absorption to a different extent, among which the enhancement of $CuBi_2O_4$ was much stronger than TiO_2 and $BiVO_4$. The difference in light-harvesting efficiency is related to the intrinsic absorption property, film compactness in addition to film thickness. Then, the promotion effect of the Ag reflective substrate on the PEC performance of these photoelectrodes was evaluated (Fig. 7b and c). A slight photocurrent enhancement of the $BiVO_4$ photoanode was achieved, with a 10% increase at 1.2 V_{RHE} (Fig. 7b). A much stronger photocurrent increase of the $CuBi_2O_4$ photocathode was observed, with an increase of 30% at 0.4 V_{RHE}. However, there was little change in the performance of TiO_2, which is reasonable since TiO_2 has a narrow absorption range in the UV region and the contribution of the light reflector was very small.

Tandem cells by connecting a photoanode and a photocathode to achieve bias-free water splitting have been regarded as an ideal path for solar conversion, which will the key direction of future research in the field.[51,52] Herein, there was a wide overlap between the polarization curves of TiO_2 photoanode and $CuBi_2O_4$ photocathode (Fig. 7c), which also have a large difference in the light absorption range (Fig. S9b and c†), a tandem cell can be constructed with TiO_2 facing at the light irradiation to utilize UV light and the rear $CuBi_2O_4$ exploiting the rest visible light (see schematic in Fig. S10†). From the UV-vis spectrum in Fig. S9d,† superimposed absorption of TiO_2 and $CuBi_2O_4$ was achieved by TiO_2//$CuBi_2O_4$. Note that when the Ag reflective substrate was integrated with the rear $CuBi_2O_4$, absorption enhancement was also achieved, indicating the availability of reflective substrate in tandem cells. Accordingly, the unbiased photocurrent of TiO_2//$CuBi_2O_4$ tandem cell along time was measured (Fig. 7d). The generated photocurrent is much lower than that in the polarization curve due to the strong light blocking of TiO_2. A 25% increase of photocurrent was achieved from 0.062 to 0.078 mA cm^{-2} when the Ag reflective substrate is adopted, which approaches that of individual $CuBi_2O_4$ photocathode. Table 1 summarizes the photocurrent density increment by Ag reflector of the recorded photoelectrodes and highlights the universal applicability and conspicuous promoting effect of adopting a reflective substance.

Table 1 List of photocurrent density with or without a Ag reflector and the photocurrent density increment by Ag reflector of the recorded photoelectrodes

Samples	$J_{electrode}$ (mA cm^{-2})	$J_{electrode+Ag}$ (mA cm^{-2})	$J_{increment}$ (%)
Fe_2O_3:Ti ($d_F = 180$ nm)[a]	1.61	1.85	15.0
TiO_2[a]	0.95	0.96	10.5
$BiVO_4$[a]	0.44	0.48	9.1
$CuBi_2O_4$[b]	−0.26	−0.35	34.6
TiO_2 + $CuBi_2O_4$[c]	0.064	0.077	20.3

[a] Bias potential of 1.23 V_{RHE}. [b] Bias potential of 0.3 V_{RHE}. [c] Bias-free photocurrent after 200 s run.

4. Conclusions

In summary, we first prepared Fe_2O_3:Ti nanorod electrodes with film thickness from 180 to 650 nm. As the film thickness increased, the light absorption efficiency was heightened but the charge transfer efficiency was essentially decreased, and thus the PEC performance reached a maximum before decreasing. The optimized film thickness of the Fe_2O_3:Ti electrode was 520 nm. To implement enhancement of light absorption, reflective substances of Cu foil, Ag foil and a mirror were adopted acting as light back-reflectors, among which the Ag foil and mirror performed equally and considerably. The promoting effect of the Ag back-reflector was decreased with increasing film thickness. With the assistance of the Ag back-reflector, the optimized film thickness of the Fe_2O_3:Ti photoanode was decreased to 290 nm, and the 260 nm-thick Fe_2O_3:Ti also exhibited a comparable performance. More importantly, the long-term durability and universal application of the Ag reflective substrate for promoting the PEC performance of $BiVO_4$ and TiO_2 photoanodes, $CuBi_2O_4$ photocathode, and TiO_2 photoanode//$CuBi_2O_4$ photocathode tandem cell were confirmed. Therefore, this simple and feasible strategy is promising for future study of the PEC system and easy for scale-up applications without limitation of device manufacturing equipment. It is noted that the reflectance of the Ag foil was merely 50% in the UV-vis range and the promoting effect on the light absorption and PEC performance of the super-thin Fe_2O_3:Ti layer (180 nm) was indeed incomplete. Therefore, seeking other powerful back-reflectors is currently underway in our group to promote the performance of the Fe_2O_3 and other photoelectrodes to a higher level.

Conflicts of interest

There are no conflicts to declare.

Acknowledgements

References

1 M. Gratzel, *Nature*, 2001, **414**, 338–344.
2 W.-Y. Yu, D.-K. Ma, D.-P. Yang, X.-G. Yang, Q.-L. Xu, W. Chen and S. Huang, *Phys. Chem. Chem. Phys.*, 2020, **22**, 20202–20211.
3 D. He, R.-T. Gao, S. Liu, M. Sun, X. Liu, K. Hu, Y. Su and L. Wang, *ACS Catal.*, 2020, **10**, 10570–10576.
4 Y. Zhang, S. Jiang, W. Song, P. Zhou, H. Ji, W. Ma, W. Hao, C. Chen and J. Zhao, *Energy Environ. Sci.*, 2015, **8**, 1231–1236.
5 F. E. Bedoya-Lora, A. Hankin, I. Holmes-Gentle, A. Regoutz, M. Nania, D. J. Payne, J. T. Cabral and G. H. Kelsall, *Electrochim. Acta*, 2017, **251**, 1–11.

6 Y. Lu, X. Ou, W. Wang, J. Fan and K. Lv, *Chin. J. Catal.*, 2020, **41**, 209–218.
7 Y. Dong and X. Fei, *Mater. Technol.*, 2020, **35**, 102–111.
8 R.-T. Gao and L. Wang, *Angew. Chem., Int. Ed.*, 2020, **59**, 23094–23099.
9 R.-T. Gao, D. He, L. Wu, K. Hu, X. Liu, Y. Su and L. Wang, *Angew. Chem., Int. Ed.*, 2020, **59**, 6213–6218.
10 H. Zhang, W. Y. Noh, F. Li, J. H. Kim, H. Y. Jeong and J. S. Lee, *Adv. Funct. Mater.*, 2019, **29**, 1805737.
11 G. Liu, Y. Zhao, R. Yao, N. Li, M. Wang, H. Ren, J. Li and C. Zhao, *Chem. Eng. J.*, 2019, **355**, 49–57.
12 B. Klahr, S. Gimenez, F. Fabregat-Santiago, T. Hamann and J. Bisquert, *J. Am. Chem. Soc.*, 2012, **134**, 4294–4302.
13 A. P. Singh, R. B. Wang, C. Tossi, I. Tittonen, B. Wickman and A. Hellman, *RSC Adv.*, 2021, **11**, 4297–4307.
14 K. Sivula, F. Le Formal and M. Grätzel, *ChemSusChem*, 2011, **4**, 432–449.
15 L. Wang, J. Zhu and X. Liu, *ACS Appl. Mater. Interfaces*, 2019, **11**, 22272–22277.
16 M. G. Ahmed, I. E. Kretschmer, T. A. Kandiel, A. Y. Ahmed, F. A. Rashwan and D. W. Bahnemann, *ACS Appl. Mater. Interfaces*, 2015, **7**, 24053–24062.
17 T. Hisatomi, F. Le Formal, M. Cornuz, J. Brillet, N. Tetreault, K. Sivula and M. Gratzel, *Energy Environ. Sci.*, 2011, **4**, 2512–2515.
18 F. Le Formal, N. Tetreault, M. Cornuz, T. Moehl, M. Gratzel and K. Sivula, *Chem. Sci.*, 2011, **2**, 737–743.
19 J. F. Zhang, R. Garcia-Rodriguez, P. Cameron and S. Eslava, *Energy Environ. Sci.*, 2018, **11**, 2972–2984.
20 J. Xiao, L. Fan, Z. Huang, J. Zhong, F. Zhao, K. Xu, S.-F. Zhou and G. Zhan, *Chin. J. Catal.*, 2020, **41**, 1761–1771.
21 Q. J. Bu, S. Li, K. Zhang, Y. H. Lin, D. J. Wang, X. X. Zou and T. F. Xie, *ACS Sustain. Chem. Eng.*, 2019, **7**, 10971–10978.
22 T.-T. Li, Q. Zhou, J. Qian, Y. Hu and Y.-Q. Zheng, *Electrochim. Acta*, 2019, **307**, 92–99.
23 J.-W. Jang, C. Du, Y. Ye, Y. Lin, X. Yao, J. Thorne, E. Liu, G. McMahon, J. Zhu, A. Javey, J. Guo and D. Wang, *Nat. Commun.*, 2015, **6**, 1–5.
24 Y. B. Park, J. H. Kim, Y. J. Jang, J. H. Lee, M. H. Lee, B. J. Lee, D. H. Youn and J. S. Lee, *ChemCatChem*, 2019, **11**, 443–448.
25 J. Xie, P. Yang, X. Liang and J. Xiong, *ACS Appl. Energy Mater.*, 2018, **1**, 2769–2775.
26 C. Wang, X. Long, S. Wei, T. Wang, F. Li, L. Gao, Y. Hu, S. Li and J. Jin, *ACS Appl. Mater. Interfaces*, 2019, **11**, 29799–29806.
27 A. Srivastav, A. Verma, A. Banerjee, S. A. Khan, M. Gupta, V. R. Satsangi, R. Shrivastav and S. Dass, *Phys. Chem. Chem. Phys.*, 2016, **18**, 32735–32743.
28 S.-S. Yi, B.-R. Wulan, J.-M. Yan and Q. Jiang, *Adv. Funct. Mater.*, 2019, **1801902**, 1–9.
29 J. Xiao, L. Fan, F. Zhao, Z. Huang, S.-F. Zhou and G. Zhan, *J. Catal.*, 2020, **381**, 139–149.
30 M. Li, Y. Yang, Y. Ling, W. Qiu, F. Wang, T. Liu, Y. Song, X. Liu, P. Fang, Y. Tong and Y. Li, *Nano Lett.*, 2017, **17**, 2490–2495.
31 K. D. Malviya, H. Dotan, D. Shlenkevich, A. Tsyganok, H. Mor and A. Rothschild, *J. Mater. Chem. A*, 2016, **4**, 3091–3099.

Paper

32 H. J. Pan, X. Y. Meng, D. Y. Liu, S. Li and G. W. Qin, *Phys. Chem. Chem. Phys.*, 2015, **17**, 22179–22186.

33 A. Kay, I. Cesar and M. Grätzel, *J. Am. Chem. Soc.*, 2006, **128**, 15714–15721.

34 M. Ji, J. Cai, Y. Ma and L. Qi, *ACS Appl. Mater. Interfaces*, 2016, **8**, 3651–3660.

35 D. Chen, Z. Liu, Z. Guo, M. Ruan and W. Yan, *Chemsuschem*, 2019, **12**, 3286–3295.

36 S. L. Bai, X. J. Yang, C. Y. Liu, X. Xiang, R. X. Luo, J. He and A. F. Chen, *ACS Sustain. Chem. Eng.*, 2018, **6**, 12906–12913.

37 L. Wang, N. T. Nguyen, X. Huang, P. Schmuki and Y. Bi, *Adv. Funct. Mater.*, 2017, **27**, 1703527.

38 I. S. Cho, H. S. Han, M. Logar, J. Park and X. Zheng, *Adv. Energy Mater.*, 2016, **6**, 1501840.

39 K. X. Wang, Z. Yu, V. Liu, M. L. Brongersma, T. F. Jaramillo and S. Fan, *ACS Photonics*, 2014, **1**, 235–240.

40 J. Li, Y. Qiu, Z. Wei, Q. Lin, Q. Zhang, K. Yan, H. Chen, S. Xiao, Z. Fan and S. Yang, *Energy Environ. Sci.*, 2014, **7**, 3651–3658.

41 K. Kim, I.-H. Kim, K.-Y. Yoon, J. Lee and J.-H. Jang, *J. Mater. Chem. A*, 2015, **3**, 7706–7709.

42 W. Wang and L. Qi, *Adv. Funct. Mater.*, 2019, **29**, 1807275.

43 Q.-D. Ou, H.-J. Xie, J.-D. Chen, L. Zhou, Y.-Q. Li and J.-X. Tang, *J. Mater. Chem. A*, 2016, **4**, 18952–18962.

44 H. Dotan, O. Kfir, E. Sharlin, O. Blank, M. Gross, I. Dumchin, G. Ankonina and A. Rothschild, *Nat. Mater.*, 2013, **12**, 158–164.

45 J. Xiao, F. Zhao, J. Zhong, Z. Huang, L. Fan, L. Peng, S.-F. Zhou and G. Zhan, *Chem. Eng. J.*, 2020, **402**, 126163.

46 J. W. Yoon, D. H. Kim, J. H. Kim, H. W. Jang and J. H. Lee, *Appl. Catal., B*, 2019, **244**, 511–518.

47 S. C. Wang, P. Chen, J. H. Yun, Y. X. Hu and L. Z. Wang, *Angew. Chem., Int. Ed.*, 2017, **56**, 8500–8504.

48 R. Chong, G. Wang, Y. Du, Y. Jia, X. Wang, C. Li, Z. Chang and L. Zhang, *Chem. Eng. J.*, 2019, **366**, 523–530.

49 S. Wang, S. Li, W. Wang, M. Zhao, J. Liu, H. Feng, Y. Chen, Q. Gu, Y. Du and W. Hao, *Sens. Actuators, B.*, 2019, **291**, 34–41.

50 K. H. Ye, H. Li, D. Huang, S. Xiao, W. Qiu, M. Li, Y. Hu, W. Mai, H. Ji and S. Yang, *Nat. Commun.*, 2019, **10**, 3687.

51 L. Pan, Y. Liu, L. Yao, R. Dan, K. Sivula, M. Grätzel and A. Hagfeldt, *Nat. Commun.*, 2020, **11**, 318.

52 S. Wang, P. Chen, Y. Bai, J. H. Yun, G. Liu and L. Wang, *Adv. Mater.*, 2018, **30**, 1800486.